Zhou, Bin, Yuhang Wang, Bin Zi, and Weidong Zhu. “Fuzzy Adaptive Whale Optimization Control Algorithm for Trajectory Tracking of a Cable-Driven Parallel Robot.” IEEE Transactions on Automation Science and Engineering, 2023, 1–12. https://doi.org/10.1109/TASE.2023.3309049.

https://doi.org/10.1109/TASE.2023.3309049

Fuzzy Adaptive Whale Optimization Control Algorithm for Trajectory Tracking of a Cable-Driven Parallel Robot

Bin Zhou, Yuhang Wang, Bin Zi, and Weidong Zhu

***Abstract*— This paper proposes a fuzzy proportion integration differentiation (PID) control strategy based on an adaptive whale optimization algorithm (FPID-AWOA) for trajectory tracking of a cable-driven parallel robot (CDPR). A mechanical prototype, and kinematic and dynamic models of the CDPR are established. Thus, new fuzzy rules are developed and a new fuzzy PID controller is designed. Subsequently, the AWOA is introduced to optimize quantization and scale factors of the fuzzy PID controller to obtain the optimal solution. Among them, AWOA is an improvement on WOA. Numerical examples show that the fuzzy PID control strategy based on adaptive whale optimization algorithm (FPID-AWOA) has higher CDPR trajectory tracking accuracy than the traditional fuzzy PID control strategy, the fuzzy PID control strategy based on whale optimization algorithm (FPID-WOA), and the fuzzy PID control strategy based on particle swarm optimization (FPID-PSOA). In comparison with the FPID and FPID-PSOA, the experimental results show that the trajectory tracking error of the proposed FPID-AWOA is reduced by 51.2% and 19.5% in the *X*-axis direction, respectively, 64.2% and 49.7% in the *Y*-axis direction, respectively, and 29.1% and 12.2% in the *Z*-axis direction, respectively.**

***Note to Practitioners*—The motivation of this article stems from the need to develop efficient trajectory tracking control algorithms for practical applications of CDPRs. Fuzzy PID control is widely used in CDPRs because of its good robustness and fast response speed. However, the fuzzy parameter selection depends on experience, and the efficiency is low. In order to obtain high quality quantization and scale factors quickly, we propose FPID-AWOA. It uses AWOA to find the optimal quantization and scale factors, which makes the fuzzy PID control get better performance. FPID-AWOA can also be applied to control other robots. In future research, we will extend the proposed approach to multiple CDPRs working collaboratively as well as to mobile operational requirements.**

***Index Terms*— Cable-driven parallel robot, fuzzy control, particle swarm optimization algorithm, trajectory tracking, whale optimization algorithm.**

I. Introduction

CABLE-DRIVEN parallel robots (CDPRs) are known as a type of mechanical structure that is actuated by cables instead of rigid links [1]. Parallel cables are widely used in CDPRs to provide constraints to realize multiple degrees of freedom [2]. CDPRs has large and easily extensible workspace, relatively simple structure, superior flexibility [3], and other cost-wise advantages based on the relatively light weight of cables compared to conventional manipulators with rigid arms [4]. Nowadays, CDPRs have been widely used in many fields such as construction [5], rehabilitation [6], telescope [7], and 3D printing [8]. However, the special structure also generates several problems in the trajectory tracking control of CDPRs [9], [10]. On one hand, the cables must be in tension because of the particular structure [11]. On the other hand, it is difficult for the current trajectory tracking control schemes to achieve satisfactory control accuracy because of modeling errors in the kinematics and dynamics [12]. Hence, it is necessary to solve these problems in the trajectory tracking control of CDPRs.

Over the years, many scholars have studied robot trajectory tracking control methods, and the more common control methods for robot trajectory tracking in general are proportion integration differentiation (PID) control, variable structure sliding mode control, compliance control, and adaptive control [13], [15]. With the continuous development of intelligent control theory and application, intelligent control methods have been widely used in robot trajectory tracking control. The robot intelligent control methods mainly include neural network control and fuzzy control [16]. Purwar et al. approximate the uncertain part of the mechanical arm structure through fuzzy control, which to some extent makes up of the disadvantage that the controller designed based on the computational torque method is difficult to control the uncertain part [17]. Mahmoodabadi et al. used a multi-objective particle swarm optimization algorithm to optimize the fuzzy controller of the nonlinear system, which improved the control accuracy of the fuzzy controller for the nonlinear system [18]. Sharma et al. designed a fractional order fuzzy PID controller to improve the trajectory tracking control accuracy for the control problem of planar dual link robots [19].

Manuscript received 10 July 2023; accepted 17 August 2023. This article was recommended for publication by Associate Editor G. Chen and Editor D. Song upon evaluation of the reviewers' comments. This work was supported in part by the National Natural Science Foundation of China under Grant 52205258 and Grant 51925502, in part by the Anhui Provincial Natural Science Foundation under Grant 2108085QE218, and in part by the Fundamental Research Funds for the Central Universities under Grant JZ2023HGTB0253. *(Corresponding author: Bin Zi.)*

Bin Zhou, Yuhang Wang, and Bin Zi are with the School of Mechanical Engineering, Hefei University of Technology, Hefei 230027, China (e-mail: bzhfut@163.com; 2732424418@qq.com; hfutzibin888@163.com).

Weidong Zhu is with the Department of Mechanical Engineering, University of Maryland Baltimore County, Baltimore, MD 21250 USA (e-mail: wzhu@umbc.edu).

Color versions of one or more figures in this article are available at https://doi.org/10.1109/TASE.2023.3309049.

Digital Object Identifier 10.1109/TASE.2023.3309049

Nowadays, many researchers have applied a fuzzy PID controller to robot trajectory tracking control [20], and there is no doubt that a fuzzy PID controller has a good control effect. A fuzzy PID controller improves the control effect of a PID controller on nonlinear factors, but the design and selection of the universe, membership function and fuzzy rules of a fuzzy controller require experience and expert knowledge, and there is the drawback of poor control effect when the design is unreasonable. Thus, in order to improve the rationality of the fuzzy PID controller and trajectory tracking control effect, some researchers propose to optimize the design parameters of the fuzzy PID controller. The optimization problem of a fuzzy controller is difficult to be described by explicit or implicit mathematical functions, so the practical complex optimization problem can be solved by a swarm intelligence optimization algorithm that does not depend on mathematical functions. Richa et al. used a genetic algorithm to optimize the PID controller parameters of the planar two-link robot, and took the weight of the overall square error and integral change square controller output as the objective function to improve the trajectory tracking performance of the robot [21]. Pizarro et al. designed a fuzzy PD controller to calculate a torque control for the dual joint robot, and adopted a genetic algorithm to optimize the membership function of the fuzzy system, which improved the control accuracy [22]. Hu et al. used an improved genetic algorithm to optimize the artificially set fuzzy rules, which avoided the problem that traditional optimization methods are prone to fall into local optimal solutions in the process of optimization [23]. The above researches mainly used optimization algorithms proposed in earlier periods to solve optimization problems. However, it can be further improved in the selection of an optimization target and the optimization effect of the optimization algorithm.

To deal with these problems of high precision trajectory tracking control of CDPRs in the existing control schemes, a fuzzy PID control strategy based on an adaptive whale optimization algorithm (FPID-AWOA) is proposed to improve the control effect of CDPRs. Firstly, based on the existing fuzzy rules and configuration characteristics, this paper establishes fuzzy rules applicable to CDPRs. Then, on the basis of fuzzy PID controller, an optimization algorithm is proposed to optimize the scale factor and quantization factor of fuzzy PID controller. Based on the whale optimization algorithm, considering its shortcomings in optimization efficiency and accuracy, this paper improves the whale optimization algorithm by introducing the weight function and differential variation interference factor to improve its optimization performance. Subsequently, the newly designed whale optimization algorithm is introduced into the fuzzy PID controller. Numerical simulations and experiments under a spiral trajectory show that the proposed the FPID-AWOA can effectively improve the tracking accuracy of the CDPR trajectory.

The remainder of this paper is organized as follows. Section II introduces the mechanical design and kinematic and dynamic modeling of the CDPR. In Section III, the fuzzy PID controller is designed based on the dynamic model with an external interference; subsequently, based on the traditional whale optimization algorithm, an adaptive whale optimization algorithm is proposed and used to optimize the quantization and scale factors of the fuzzy PID controller. The simulations and experiments are carried out on the CDPR in Sections IV and V, respectively. Finally in Section VI, some conclusions are given.

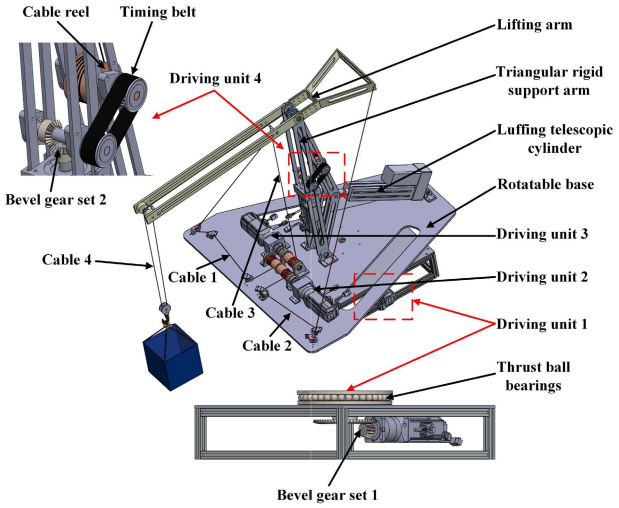

Fig. 1. Mechanical prototype of the CDPR.

II. Kinematic and Dynamic Modeling

In this section, a mechanical prototype of the CDPR is introduced., and its kinematic and dynamic models are established.

A. Mechanical Design

As shown in Fig. 1, the mechanical model of the CDPR for lifting payloads is designed. The CDPR consists of a lifting arm, a triangular rigid support arm, a luffing telescopic cylinder, a rotatable base, four driving units, four cables, two bevel gear sets, a cable reel, thrust ball bearings, and a timing belt. The CDPR has four degrees of freedom, which are provided by the four driving units and the luffing telescopic cylinder. The rotatable base connecting with thrust ball bearings is driven by the driving unit 1. The rotation function of the rotatable base is achieved by the motor torque transmitted by the bevel gear set 1. The driving units 2 and 3, the triangular rigid support arm, and the luffing telescopic cylinder are installed on the rotatable base. The triangular rigid support arm rotates through the telescopic movement of the luffing telescopic cylinder. The lifting arm is connected with the triangular rigid support arm and driven by the driving units 2 and 3 through the cables 1, 2, and 3. The driving unit 4 is fixed on the triangular rigid support arm. The retraction of cable 4 is realized by the transmission of the motor torque to the cable reel by the bevel gear set 2 and the timing belt.

B. Kinematic Modeling

The kinematic model of the CDPR is shown in Fig. 2. A global coordinate system $O-XYZ$ is located at the rotation center of the rotatable base. A moving coordinate system $O_1-X_1Y_1Z_1$ is located at the rotation center of the rotatable

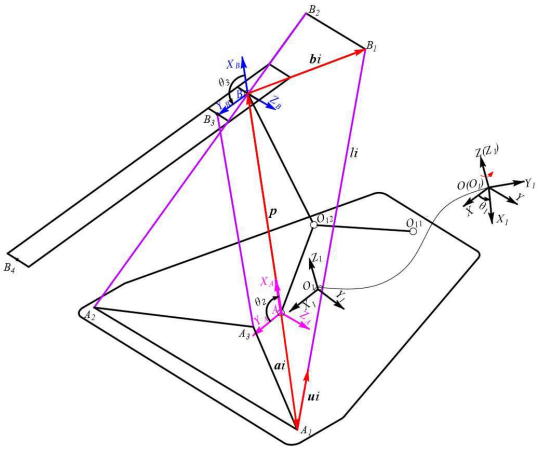

Fig. 2. Kinematic model of the CDPR.

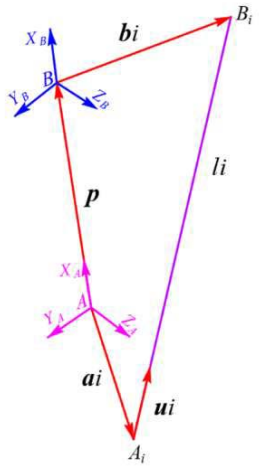

Fig. 3. Vector diagram of cable length.

base. Moving coordinate systems $A-X_AY_AZ_A$ and $B-X_BY_BZ_B$ are located at the pivot centers of the triangular rigid support arm and the lifting arm, respectively. According to the Denavit and Hartenberg theory [24], the transformation matrices ${}^{O}_{O_1}\boldsymbol{T}$, ${}^{O}_{A}\boldsymbol{T}$, and ${}^{O}_{B}\boldsymbol{T}$ are expressed as

$$ {}^{O}_{O_1}\boldsymbol{T} = \begin{bmatrix} c\theta_1 & -s\theta_1 & 0 & 0 \\ s\theta_1 & c\theta_1 & 0 & 0 \\ 0 & 0 & 1 & 0 \\ 0 & 0 & 0 & 1 \end{bmatrix} \tag{1} $$

$$ {}^{O}_{A}\boldsymbol{T} = {}^{O}_{O_1}\boldsymbol{T} \cdot {}^{O_1}_{A}\boldsymbol{T} = \begin{bmatrix} c\theta_1 c\theta_2 & -c\theta_1 s\theta_2 & -s\theta_1 & l_{O1A}c\theta_1 \\ s\theta_1 c\theta_2 & -s\theta_1 c\theta_1 & c\theta_1 & l_{O1A}s\theta_1 \\ -s\theta_2 & -c\theta_2 & 0 & 0 \\ 0 & 0 & 0 & 1 \end{bmatrix} \tag{2} $$

$$ \begin{aligned} {}^{O}_{B}\boldsymbol{T} &= {}^{O}_{O_1}\boldsymbol{T} \cdot {}^{O_1}_{A}\boldsymbol{T} \cdot {}^{A}_{B}\boldsymbol{T} \\ &= \begin{bmatrix} c\theta_1 c\theta_2 c\theta_3 - c\theta_1 s\theta_2 s\theta_3 & -c\theta_1 c\theta_2 s\theta_3 - c\theta_1 s\theta_2 c\theta_3 & -s\theta_1 & l_{O1A}c\theta_1 + l_{AB}c\theta_1 c\theta_2 \\ s\theta_1 c\theta_2 c\theta_3 - s\theta_1 s\theta_2 s\theta_3 & s\theta_1 c\theta_2 s\theta_3 - s\theta_1 s\theta_2 c\theta_3 & c\theta_1 & l_{O1A}s\theta_1 + l_{AB}s\theta_1 c\theta_2 \\ -c\theta_2 s\theta_3 - s\theta_2 c\theta_3 & s\theta_2 s\theta_3 - c\theta_2 c\theta_3 & 0 & -l_{AB}s\theta_2 \\ 0 & 0 & 0 & 1 \end{bmatrix} \end{aligned} \tag{3} $$

respectively, where θ_1, θ_2, and θ_3 are rotational angles, l_{O1A} is the length between points O_1 and A, and l_{AB} is the length between points A and B. Notice that "s" and "c" represent "*sin*" and "*cos*", respectively.

The vector diagram of cable length of the CDPR is shown in Fig. 3, where $\boldsymbol{a_i}$ is the position vector of the point A_i in the moving coordinate system $A-X_AY_AZ_A$, $\boldsymbol{p}$ is the position vector of the triangular rigid support arm in the moving coordinate system $A-X_AY_AZ_A$, $\boldsymbol{b_i}$ is the position vector of the point B_i in the moving coordinate system $B-X_BY_BZ_B$, and $\boldsymbol{u_i}$ is the unit direction vector along the cable direction. Based on the Eqs. (1)-(3), one has

$$ l_i = \|\boldsymbol{l_i}\| = \sqrt{(\boldsymbol{p}+\boldsymbol{b_i}-\boldsymbol{a_i})^T(\boldsymbol{p}+\boldsymbol{b_i}-\boldsymbol{a_i})}, \quad i = 1,2,3 \tag{4} $$

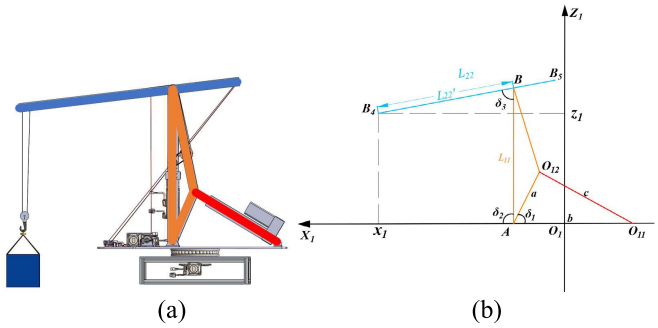

(a) (b)

Fig. 4. Side view and geometrical relationship of the CDPR: (a) Side view and (b) geometrical relationship.

where l_i represents the ith cable length; $\boldsymbol{l_i}$ represents the ith cable length vector.

Suppose the position coordinate of the point B_4 in the $O-XYZ$ is expressed as (x, y, z). Thus, the θ_1 can be calculated by

$$ \theta_1 = arctan\left(\frac{y}{x}\right) \tag{5} $$

To solve other poses of the CDPR, the triangular rigid support arm and the lifting arm can be considered as a two-link mechanism with two degrees of freedom. As shown in Fig. 4, ABO_{12} represents the triangular rigid support arm, B_4B_5 represents the lifting arm, and $O_{11}O_{12}$ represents the luffing telescopic cylinder. According to the geometric method and cosine theorem [25], the intersection angels δ_1, δ_2, and δ_3 are expressed as

$$ \delta_1 = \cos^{-1}\left(\frac{a^2+b^2-c^2}{2\cdot a\cdot b}\right) \tag{6} $$

$$ \delta_2 = \cos^{-1}\left(\frac{L_{11}^2+\left(x_1-l_{AO_1}\right)^2+z_1^2-L_{22'}^2}{2\cdot L_{11}\cdot\sqrt{\left(x_1-l_{AO_1}\right)^2+z_1^2}}\right) + \tan^{-1}\left(\frac{z_1}{x_1-l_{AO_1}}\right) \tag{7} $$

$$ \delta_3 = \cos^{-1}\left(\frac{L_{11}^2+L_{22'}^2-\left(x_1-l_{AO_1}\right)^2-z_1^2}{2\cdot L_{11}\cdot L'_{22}}\right) \tag{8} $$

where x_1 and z_1 are the coordinates of the point B_4 along X_1-axis and Z_1-axis in the $O_1-X_1Y_1Z_1$, and $x_1=\sqrt{x^2+y^2}$, $z_1=z$; L_{11} is the length of AB; L_{22} is the length of B_4B_5; L'_{22} is the length of BB_4; and l_{AO_1} is the length of AO_1. Based on Eqs. (7) and (8), the θ_2 and θ_3 can be calculated by

$$\theta_2=-\delta_2 \tag{9}$$

$$\theta_3=\frac{\pi}{2}-\delta_3 \tag{10}$$

where δ_2 is the intersection angle between AB and X_1-axis; and δ_3 is the intersection angle between AB and BB_4.The expansion amount of the luffing telescopic cylinder Δx can be calculated by

$$\begin{aligned}\Delta x &= c-c_0\\ &=\sqrt{a^2+b^2-2\cdot a\cdot b\cdot cos\delta_1}-\sqrt{a^2+b^2-2\cdot a\cdot b\cdot cos\delta_1'}\end{aligned} \tag{11}$$

where δ_1 is the intersection angle between AO_{11} and AO_{12}; δ_1' is the value of δ_1 when the triangular rigid support arm is vertical; a is the length of AO_{12}; b is the length of AO_{11}; c is the length of $O_{11}O_{12}$; and c_0 is the length of $O_{11}O_{12}$ when the triangular rigid support arm is vertical.

C. Dynamic Modeling

It is assumed that the robot is well lubricated and the frictional force for the whole robot system can be neglected. The rotatable base, triangular rigid support arm, and lifting arm of the CDPR are simplified as a three-link mechanism. As shown in Fig. 2, the coordinates of the center of the rotatable base along the X-axis, Y-axis, and Z-axis in the moving coordinate system $O_1-X_1Y_1Z_1$ are denoted as (x_1, y_1, z_1); the coordinates of the center of the triangular rigid support arm along the X-axis, Y-axis, and Z-axis in the moving coordinate system $A-X_AY_AZ_A$ are denoted as (x_2, y_2, z_2); the coordinates of center of lifting arm along the X-axis, Y-axis, and Z-axis in the moving coordinate system $B-X_BY_BZ_B$ are denoted as (x_3, y_3, z_3), and the coordinates of the center of the payload along the X-axis, Y-axis, and Z-axis in the moving coordinate system $B-X_BY_BZ_B$ are denoted as (x_4, y_4, z_4). Thus, the position vector of the center of the rotatable base ${}^{O_1}\boldsymbol{r}_1$ is expressed as

$${}^{O_1}\boldsymbol{r}_1=\begin{pmatrix} x_1 & y_1 & z_1 & 1\end{pmatrix}^T \tag{12}$$

The position vector of the center of the triangular rigid support arm ${}^{A}\boldsymbol{r}_2$ is expressed as

$${}^{A}\boldsymbol{r}_2=\begin{pmatrix} x_2 & y_2 & z_2 & 1\end{pmatrix}^T \tag{13}$$

The position vector of the center of the lifting arm ${}^{B}\boldsymbol{r}_3$ is expressed as

$${}^{B}\boldsymbol{r}_3=\begin{pmatrix} x_3 & y_3 & z_3 & 1\end{pmatrix}^T \tag{14}$$

The position vector of the center of the payload ${}^{B}\boldsymbol{r}_4$ is expressed as

$${}^{B}\boldsymbol{r}_4=\begin{pmatrix} x_4 & y_4 & z_4 & 1\end{pmatrix}^T \tag{15}$$

For simplification, note that ${}^{O_1}\boldsymbol{r}_1$, ${}^{A}\boldsymbol{r}_2$, ${}^{B}\boldsymbol{r}_3$, and ${}^{B}\boldsymbol{r}_4$ are denoted as ${}^{1}\boldsymbol{r}_1$, ${}^{2}\boldsymbol{r}_2$, ${}^{3}\boldsymbol{r}_3$, and ${}^{4}\boldsymbol{r}_4$, respectively. By taking derivatives of Eqs. (12)-(15), the velocity vectors ${}^{0}\boldsymbol{v}_i$ of centers of the rotatable base, triangular rigid support arm, lifting arm, and payload relative to the $O-XYZ$ coordinate system are expressed as

$$\begin{aligned}&{}^{O}\boldsymbol{v}_i=\frac{d}{dt}\left({}^{O}\boldsymbol{r}_i\right)=\frac{d}{dt}\left({}_i^O\boldsymbol{T}\cdot{}^{i}\boldsymbol{r}_i\right)=\left(\sum_{j=1}^{i}\frac{\partial_i^O\boldsymbol{T}}{\partial\theta_j}\cdot\dot{\theta_j}\right)\cdot{}^{i}\boldsymbol{r}_i,\\ &{}_i^O\boldsymbol{T}={}_{O_1}^O\boldsymbol{T},i=1;{}_i^O\boldsymbol{T}={}_A^O\boldsymbol{T},i=2;{}_i^O\boldsymbol{T}={}_B^O\boldsymbol{T},i=3,4\end{aligned} \tag{16}$$

where ${}^{O}\boldsymbol{v}_i$ represent the velocity vectors of centers of the rotatable base, triangular rigid support arm, lifting arm, and payload relative to the global coordinate system $O-XYZ$; ${}^{O}\boldsymbol{r}_i$ represents position vectors of centers of the rotatable base, triangular rigid support arm, lifting arm, and payload relative to the global coordinate system $O-XYZ$. Based on Eq. (16), the kinetic energy K_i of centers of the rotatable base, triangular rigid support arm, lifting arm, and payload can be calculated by

$$\begin{aligned}K_i&=\frac{1}{2}m_i\cdot tr\left({}^{O}\boldsymbol{v}_i,{}^{O}\boldsymbol{v}_i^T\right)\\ &=\frac{1}{2}m_i\cdot tr\left[\sum_{j=1}^{i}\sum_{k=1}^{i}\frac{\partial\left({}_i^O\boldsymbol{T}\right)}{\partial\theta_j}{}^{i}\boldsymbol{r}_i\cdot\left({}^{i}\boldsymbol{r}_i\right)^T\frac{\partial\left({}_i^O\boldsymbol{T}\right)^T}{\partial\theta_k}\dot{\theta}_j\dot{\theta}_k\right]\\ &=\frac{1}{2}m_i\cdot tr\left[\sum_{j=1}^{i}\sum_{k=1}^{i}\frac{\partial\left({}_i^O\boldsymbol{T}\right)}{\partial\theta_j}{}^{i}\boldsymbol{r}_i\cdot\left({}^{i}\boldsymbol{r}_i\right)^T\frac{\partial\left({}_i^O\boldsymbol{T}\right)^T}{\partial\theta_k}\dot{\theta}_j\dot{\theta}_k\right]\end{aligned} \tag{17}$$

where K_1, K_2, K_3, and K_4 represent the kinetic energy of centers of the rotatable base, triangular rigid support arm, lifting arm, and payload, respectively, and

$$\begin{cases}K_1=\frac{1}{2}m_1{}^{O}v_1^2\\ K_2=\frac{1}{2}m_2{}^{O}v_2^2\\ K_3=\frac{1}{2}m_3{}^{O}v_3^2\\ K_4=\frac{1}{2}m_4{}^{O}v_4^2\end{cases} \tag{18}$$

where m_1, m_2, m_3, and m_4 represent the masses of the rotatable base, triangular rigid support arm, lifting arm, and payload, respectively; ${}^{O}\boldsymbol{v}_1$,${}^{O}\boldsymbol{v}_2$,${}^{O}\boldsymbol{v}_3$, and ${}^{O}\boldsymbol{v}_4$ represent the linear velocity vectors of the center of the rotatable base relative to the global coordinate system $O-XYZ$. Thus, based on Eq. (18), the total kinetic energy of the CDPR can be calculated by

$$K=\sum\nolimits_{i=1}^{4}K_i \tag{19}$$

Subsequently, the $O-XY$ plane is chosen as the zero potential energy surface. Thus, the potential energy of the rotatable base, triangular rigid support arm, lifting arm, and payload can be calculated by

$$\begin{cases}U_1=0\\ U_2=m_2g^0h_{z_2}\\ U_3=m_3g^0h_{z_3}\\ U_4=m_4g^0h_{z_4}\end{cases} \tag{20}$$

where g is gravitational acceleration; ${}^0h_{z_2}$, ${}^0h_{z_3}$, and ${}^0h_{z_4}$ are respectively the components of the centroid coordinates of triangular rigid support arm, lifting arm, and payload relative to the Z-axis on the $O-XYZ$. Thus, based on Eq. (20), the total potential energy of the CDPR can be calculated by

$$U=\sum_{i=1}^{4}U_i \tag{21}$$

In many control systems, cables are often simplified for ease of analysis and control design. The focus is primarily on the primary dynamics of the system, ignoring the smaller deformations caused by flexible cables. In addition, the deformation of flexible cables has a very small effect on the control performance, and the relatively small flexibility of the cable is such that its deformation does not significantly affect the overall behavior or stability of the controlled system. Therefore, this paper ignores the cable deformation.

Based on the Lagrange dynamic formulation [26] and Eqs. (19) and (21), one has

$$L=K-U=\sum_{i=1}^{4}(K_i-U_i) \tag{22}$$

By taking derivatives of Eq. (22), the dynamics equation for the CDPR can be expressed as

$$\tau_i=\frac{d}{dt}\frac{\partial L}{\partial\dot{\theta}_i}-\frac{\partial L}{\partial\theta_i}=\frac{d}{dt}\frac{\partial K}{\partial\dot{\theta}_i}-\frac{\partial K}{\partial\theta_i}+\frac{\partial U}{\partial\theta_i} \tag{23}$$

where τ_i is the torque of each joint. For simplification, Eq. (23) is written as

$$\boldsymbol{\tau}=\boldsymbol{M}(\boldsymbol{\Theta})\ddot{\boldsymbol{\Theta}}+\boldsymbol{C}\left(\dot{\boldsymbol{\Theta}},\boldsymbol{\Theta}\right)\dot{\boldsymbol{\Theta}}+\boldsymbol{G}(\boldsymbol{\Theta}) \tag{24}$$

where $\boldsymbol{\Theta}=\left[\theta_1\ \theta_2\ \theta_3\right]^T$ is the joint angle vector; $\boldsymbol{M}(\boldsymbol{\Theta})\in R^{3\times3}$ is the inertia matrix; $\boldsymbol{C}\left(\dot{\boldsymbol{\Theta}},\boldsymbol{\Theta}\right)\dot{\boldsymbol{\Theta}}\in R^3$ is the centrifugal and Coriolis force matrix; $\boldsymbol{G}(\boldsymbol{\Theta})\in R^3$ is the gravity matrix.

III. Fuzzy Trajectory Tracking Control

In this section, a numerical method is used to solve the problem that the dynamic equation cannot be expressed in detail. Then, an adaptive whale optimization algorithm is applied to the fuzzy PID controller.

A. Numerical Solutions to Dynamic Model

Obviously, based on Eq. (24), the acceleration $\ddot{\boldsymbol{\Theta}}_t$ at time t is expressed as

$$\ddot{\boldsymbol{\Theta}}_t=\boldsymbol{M}^{-1}(\boldsymbol{\Theta}_t)\left[\boldsymbol{\tau}_t-\boldsymbol{C}\left(\dot{\boldsymbol{\Theta}}_t,\boldsymbol{\Theta}_t\right)\dot{\boldsymbol{\Theta}}_t-\boldsymbol{G}(\boldsymbol{\Theta}_t)\right] \tag{25}$$

where $\boldsymbol{\Theta}_t$, $\dot{\boldsymbol{\Theta}}_t$, and $\ddot{\boldsymbol{\Theta}}_t$ are angle, angular velocity, and angular acceleration vectors of joints at time t; and $\boldsymbol{\tau}_t$ is the joint torque at time t. When the number of joints is 2, the mathematical functions of $\boldsymbol{M}(\boldsymbol{\Theta})$, $\boldsymbol{C}\left(\dot{\boldsymbol{\Theta}},\boldsymbol{\Theta}\right)\dot{\boldsymbol{\Theta}}$, and $\boldsymbol{G}(\boldsymbol{\Theta})$ matrix elements can be expressed easily, but when the number of joints is greater than 2, the mathematical functions of $\boldsymbol{M}(\boldsymbol{\Theta})$, $\boldsymbol{C}\left(\dot{\boldsymbol{\Theta}},\boldsymbol{\Theta}\right)\dot{\boldsymbol{\Theta}}$, and $\boldsymbol{G}(\boldsymbol{\Theta})$ matrix elements become complex and lengthy and not easy to derive; however, values of $\boldsymbol{M}(\boldsymbol{\Theta})$, $\boldsymbol{C}\left(\dot{\boldsymbol{\Theta}},\boldsymbol{\Theta}\right)\dot{\boldsymbol{\Theta}}$, and $\boldsymbol{G}(\boldsymbol{\Theta})$ at time t can be numerically calculated. Thus, Eq. (24) can be expanded in another form:

$$\begin{bmatrix}\tau_1\\ \tau_2\\ \tau_3\end{bmatrix}=\begin{bmatrix}\boldsymbol{M}_{11}&\boldsymbol{M}_{12}&\boldsymbol{M}_{13}\\ \boldsymbol{M}_{21}&\boldsymbol{M}_{22}&\boldsymbol{M}_{23}\\ \boldsymbol{M}_{31}&\boldsymbol{M}_{32}&\boldsymbol{M}_{33}\end{bmatrix}\begin{bmatrix}\ddot{\theta}_1\\ \ddot{\theta}_2\\ \ddot{\theta}_3\end{bmatrix}+\begin{bmatrix}\boldsymbol{C}_{11}&\boldsymbol{C}_{12}&\boldsymbol{C}_{13}\\ \boldsymbol{C}_{21}&\boldsymbol{C}_{22}&\boldsymbol{C}_{23}\\ \boldsymbol{C}_{31}&\boldsymbol{C}_{32}&\boldsymbol{C}_{33}\end{bmatrix}\begin{bmatrix}\dot{\theta}_1\\ \dot{\theta}_2\\ \dot{\theta}_3\end{bmatrix}+\begin{bmatrix}\boldsymbol{G}_1\\ \boldsymbol{G}_2\\ \boldsymbol{G}_3\end{bmatrix} \tag{26}$$

According to Eq. (26), all elements in $\boldsymbol{M}(\boldsymbol{\Theta})$ are a function of $\boldsymbol{\Theta}$ and independent of $\dot{\boldsymbol{\Theta}}$, $\ddot{\boldsymbol{\Theta}}$, and g; all elements in $\boldsymbol{C}\left(\dot{\boldsymbol{\Theta}},\boldsymbol{\Theta}\right)$ are a function of $\dot{\boldsymbol{\Theta}}$ and $\boldsymbol{\Theta}$ and independent of $\ddot{\boldsymbol{\Theta}}$, and g; and all elements in $\boldsymbol{G}(\boldsymbol{\Theta})$ are a function of $\boldsymbol{\Theta}$ and g and independent of $\dot{\boldsymbol{\Theta}}$, and $\ddot{\boldsymbol{\Theta}}$. Thus, one sets $\ddot{\boldsymbol{\Theta}}=\begin{bmatrix}1\\0\\0\end{bmatrix}$, $\dot{\boldsymbol{\Theta}}=\begin{bmatrix}0\\0\\0\end{bmatrix}$, $\boldsymbol{\Theta}=\begin{bmatrix}\theta_1\\ \theta_2\\ \theta_3\end{bmatrix}$, $g=0$, and based on Eq. (26), one has

$$\begin{bmatrix}\tau_1\\ \tau_2\\ \tau_3\end{bmatrix}=\begin{bmatrix}\boldsymbol{M}_{11}&\boldsymbol{M}_{12}&\boldsymbol{M}_{13}\\ \boldsymbol{M}_{21}&\boldsymbol{M}_{22}&\boldsymbol{M}_{23}\\ \boldsymbol{M}_{31}&\boldsymbol{M}_{32}&\boldsymbol{M}_{33}\end{bmatrix}\begin{bmatrix}1\\0\\0\end{bmatrix}+\begin{bmatrix}0\\0\\0\end{bmatrix}+\begin{bmatrix}0\\0\\0\end{bmatrix}=\begin{bmatrix}\boldsymbol{M}_{11}\\ \boldsymbol{M}_{21}\\ \boldsymbol{M}_{31}\end{bmatrix} \tag{27}$$

Similarly, one sets $\ddot{\boldsymbol{\Theta}}=\begin{bmatrix}0\\1\\0\end{bmatrix}$, and based on Eq. (26), one has $\begin{bmatrix}\tau_1\\ \tau_2\\ \tau_3\end{bmatrix}=\begin{bmatrix}\boldsymbol{M}_{12}\\ \boldsymbol{M}_{22}\\ \boldsymbol{M}_{32}\end{bmatrix}$; one sets $\ddot{\boldsymbol{\Theta}}=\begin{bmatrix}0\\0\\1\end{bmatrix}$, and based on Eq. (26), one has $\begin{bmatrix}\tau_1\\ \tau_2\\ \tau_3\end{bmatrix}=\begin{bmatrix}\boldsymbol{M}_{13}\\ \boldsymbol{M}_{23}\\ \boldsymbol{M}_{33}\end{bmatrix}$. Similarly, one sets $\ddot{\boldsymbol{\Theta}}=\begin{bmatrix}0\\0\\0\end{bmatrix}$, $\dot{\boldsymbol{\Theta}}=\begin{bmatrix}\dot{\theta}_1\\ \dot{\theta}_2\\ \dot{\theta}_3\end{bmatrix}$, $\boldsymbol{\Theta}=\begin{bmatrix}\theta_1\\ \theta_2\\ \theta_3\end{bmatrix}$, and $g=9.8$, and based on Eq. (26), one has

$$\begin{bmatrix}\tau_1\\ \tau_2\\ \tau_3\end{bmatrix}=\begin{bmatrix}0\\0\\0\end{bmatrix}+\begin{bmatrix}\boldsymbol{C}_{11}&\boldsymbol{C}_{12}&\boldsymbol{C}_{13}\\ \boldsymbol{C}_{21}&\boldsymbol{C}_{22}&\boldsymbol{C}_{23}\\ \boldsymbol{C}_{31}&\boldsymbol{C}_{32}&\boldsymbol{C}_{33}\end{bmatrix}\begin{bmatrix}\dot{\theta}_1\\ \dot{\theta}_2\\ \dot{\theta}_3\end{bmatrix}+\begin{bmatrix}\boldsymbol{G}_1\\ \boldsymbol{G}_2\\ \boldsymbol{G}_3\end{bmatrix} \tag{28}$$

Based on Eqs. (26)-(28), the values of $\boldsymbol{M}(\boldsymbol{\Theta}_t)$ and $\boldsymbol{C}\left(\dot{\boldsymbol{\Theta}}_t,\boldsymbol{\Theta}_t\right)\dot{\boldsymbol{\Theta}}_t+\boldsymbol{G}(\boldsymbol{\Theta}_t)$ in Eq. (25) can be calculated.

B. Fuzzy PID Controller

In the fuzzy PID controller, the error e_j and error rate e_{cj} of each joint angle are considered as input variables of the fuzzy controller, and one has

$$e_j=\theta_{dj}-\theta_j,\ j=1,2,3 \tag{29}$$

$$e_{cj}=\dot{\theta_{dj}}-\dot{\theta_j} \tag{30}$$

where θ_{dj} is the ideal joint angle; θ_j is the actual joint angle; $\dot{\theta_{dj}}$ is the ideal angular velocity vector; and $\dot{\theta_j}$ is the actual

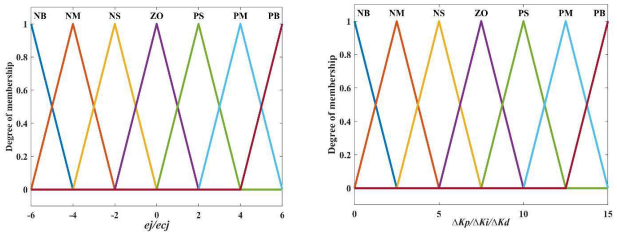

(a) (b)

Fig. 5. Curves of membership functions of the input and output variables: (a) e_j and e_{cj}, and (b) ΔK_p, ΔK_i, and ΔK_d.

angular velocity vector. According to the fuzzy theory, the membership degrees of e_j and e_{cj} with respect to different fuzzy subsets are obtained. Subsequently, outputs ΔK_p, ΔK_i, and ΔK_d of the fuzzy PID controller are obtained by the fuzzy algorithm. Thus, the fuzzy PID controller is adaptively adjusted by ΔK_p, ΔK_i, and ΔK_d, and the output torque $\tau_j(t)$ is expressed as

$$\begin{aligned}\tau_j(t) &= \left(K_{po}+\Delta K_p\right)e_j + \left(K_{io}+\Delta K_i\right)\int_0^t e_j dt + \left(K_{do}+\Delta K_d\right)\frac{de_j}{dt} \\ &= \left(K_{po}e_j + K_{io}\int_0^t e_j dt + K_{do}\frac{de_j}{dt}\right) + \left(\Delta K_p e_j \right. \\ &\quad \left. + \Delta K_i \int_0^t e_j dt + \Delta K_d \frac{de_j}{dt}\right) \end{aligned} \tag{31}$$

where K_{po}, K_{io}, and K_{do} are the initial values of PID in the artificially selected fuzzy PID controller.

It should be noticed that the more the number of fuzzy subsets, the higher the control accuracy and the more the control cost [27], [28]. Thus, the numbers of fuzzy subsets of the input variables including the error e_j, the error rate e_{cj}, and the output variables such as ΔK_p, ΔK_i, and ΔK_d are 7. The curves of membership functions of the input variables including the error e_j, the error rate e_{cj}, and the output variables such as ΔK_p, ΔK_i, and ΔK_d are shown in Fig. 5. The ranges of variation of e_j and e_{cj} are both $[-6, 6]$, the fuzzy subsets of e_j and e_{cj} are NB: negative bigness, NM: negative medium, NS: negative small, ZO: zero, PS: positive small, PM: positive medium, and PB: positive bigness. Meanwhile, the ranges of variation of ΔK_p, ΔK_i, and ΔK_d are $[0, 15]$, the fuzzy subsets of ΔK_p, ΔK_i, and ΔK_d are also NB: negative bigness, NM: negative medium, NS: negative small, ZO: zero, PS: positive small, PM: positive medium, and PB: positive bigness. The fuzzy regular surface diagrams of ΔK_p, ΔK_i and ΔK_d are shown in Fig. 6. Based on the centroid method [29] and Figs. 5 and 6, the ΔK_p, ΔK_i, and ΔK_d of the fuzzy PID controller can be calculated by

$$\mu_j = \frac{\sum_{j=0}^{n} \mu_c(z_j) \cdot z_j}{\sum_{j=0}^{n} \mu_c(z_j)} \tag{32}$$

where μ_j are the exact values of the output variables of the fuzzy controller after defuzzification, z_j are the values of

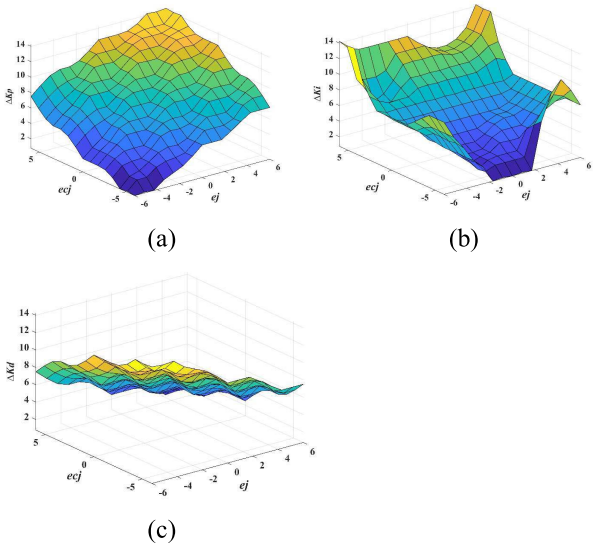

(a) (b) (c)

Fig. 6. Fuzzy regular surface diagrams: (a) ΔK_p (b) ΔK_i, and (c) ΔK_d.

fuzzy control quantity in the fuzzy field, and $\mu_c(z_j)$ are the membership values of z_j.

C. Fuzzy Control Strategy Based on an Adaptive Whale Optimization Algorithm

It should be noticed that the quantization factor and scale factor of fuzzy controller will seriously affect the dynamic and static quality and stability of the system. The values of quantization factors K_{e_j}, $K_{e_{cj}}$ and scale factors $K_{u_{p_j}}$, $K_{u_{i_j}}$, and $K_{u_{d_j}}$ are judged and selected through experience. Thus, an adaptive whale optimization algorithm is selected to optimize the K_{e_j}, $K_{e_{cj}}$ and $K_{u_{p_j}}$, $K_{u_{i_j}}$, and $K_{u_{d_j}}$ of the fuzzy PID controller to improve the stability and accuracy of the control system.

In the global search stage, whale optimization algorithm (WOA) randomly selects an individual as the lucky individual in the population, whose position is defined as $X_{rand}(t)$, and other individuals will move to the selected lucky individual. The current position of individual whale is defined as $X(t)$, and the step size of individual movement D_1 is expressed as

$$D_1 = |C \cdot X_{rand}(t) - X(t)| \tag{33}$$

$$X(t+1) = X_{rand}(t) - A \cdot D_1 \tag{34}$$

where $X(t+1)$ is the updated position of the individual whale; A and C are coefficients, and

$$A = 2a \cdot r_1 - a \tag{35}$$

$$C = 2 \cdot r_2 \tag{36}$$

$$a = 2 - \frac{2t}{T_{max}} \tag{37}$$

in which a is the control parameter of the algorithm, and with the increase of the number of iterations, the value of a decreases from 2 to 0, and the decreasing trend is linear; r_1 and r_2 are random numbers between $[0, 1]$; t represents the current number of iterations; and T_{max} is the maximum

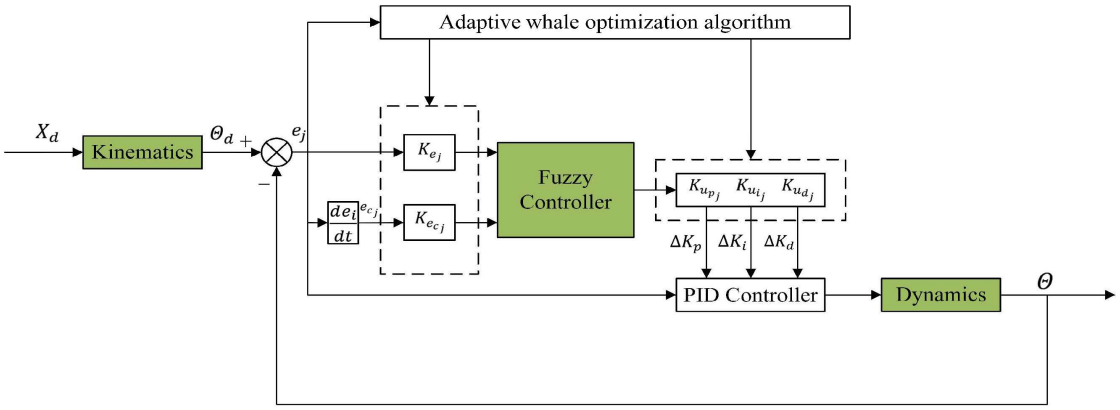

Fig. 7. The control diagram of the proposed FPID-AWOA.

number of iterations. In the local optimization stage, WOA selects an individual as the best individual in the population, whose position is defined as $X_{best}(t)$, the remaining individuals will move to $X_{best}(t)$, and the step size of individual movement is expressed as

$$D_2 = |C \cdot X_{best}(t) - X(t)| \tag{38}$$

The distance D' from $X_{best}(t)$ to $X(t)$ is expressed as

$$D' = |X_{best}(t) - X(t)| \tag{39}$$

Based on Eqs. (38) and (39), $X(t+1)$ is expressed as

$$X(t+1) = \begin{cases} X_{best}(t) - A \cdot D_2 \\ D' \cdot e^{bl} \cdot \cos(2\pi l) + X_{best}(t) \end{cases} \tag{40}$$

where b is a constant coefficient; and l is a random number between $[-1, 1]$. Based on Eqs. (34) and (40), when the probability factor $p \geq 0.5$, $X(t+1)$ is expressed as

$$X(t+1) = D' \cdot e^{bl} \cdot \cos(2\pi l) + X_{best}(t) \tag{41}$$

when the probability factor $p < 0.5$, $X(t+1)$ is expressed as

$$X(t+1) = \begin{cases} X_{rand}(t) - A \cdot D_1 & |A| \geq 1 \\ X_{best}(t) - A \cdot D_2 & |A| < 1 \end{cases} \tag{42}$$

A weight function and a differential mutation interference factor are introduced into WOA because of its slow convergence rate, low solving accuracy, and easily falling into local optimal. The weight function ω is introduced to control the updating position of whales, and

$$\omega = \omega_{max} - (\omega_{max} - \omega_{min}) \left(\frac{t}{T_{max}} \right)^{\frac{1}{7}} \tag{43}$$

where the range of ω is $[\omega_{min}, \omega_{max}]$. Based on Eqs. (41) and (42), and by introducing the weight ω, one has

$$X(t+1) = \omega \cdot D' \cdot e^{bl} \cdot \cos(2\pi l) + X_{best}(t) \tag{44}$$

$$X(t+1) = X_{rand}(t) - \omega \cdot A \cdot D_1 \tag{45}$$

In addition, the differential mutation interference factor γ is introduced, and

$$\gamma = \delta \cdot (X_{best}(t) - X(t)) \tag{46}$$

where δ is an adaptive mutation factor, and

$$\delta = \delta_0 \cdot 2^{\varepsilon} \tag{47}$$

$$\varepsilon = e^{1 - \frac{T_{max}}{T_{max}+1-t}} \tag{48}$$

in which δ_0 is the mutation parameter. At the initial stage, and $\delta = 2\delta_0$. The value of δ gradually approaches δ_0 with the increase of the number of iterations, which makes WOA easier to jump out of the local optimal solution and avoid premature. Based on Eq. (42) and by introducing the differential variation interference factor γ, one has

$$X(t+1) = X_{best}(t) - A \cdot D_2 + \gamma \tag{49}$$

Compared with other optimization algorithms, AWOA has the advantages of simple operation, fewer parameters to be adjusted, better convergence speed and global search capability, as well as the ability to jump out of the local optimum, high solution accuracy, fast finding of optimal solutions, and effective working for various types of optimization problems. Therefore, this paper chooses to optimize the fuzzy PID controller by AWOA. The control diagram of the proposed FPID-AWOA is shown in Fig. 7. The ideal trajectory X_d in the Cartesian space is transformed into the ideal joint angle in the joint space by kinematics, and the error between the ideal joint angle and the actual joint angle and the error change rate are used as inputs to optimize the fuzzy parameters by the designed AWOA to obtain the optimal PID parameters, and then control the robot to achieve high precision trajectory tracking.

IV. Numerical Simulations

In this section, in order to observe the control performance of the proposed FPID-AWOA, the system simulation test is carried out, and the trajectory tracking control performances of FPID, FPID-WOA, FPID-PSOA, and FPID-AWOA are compared and analyzed.

By considering the limit position that the robot can reach and the experimental effect, as shown in Fig. 8, and assuming that the trajectory of point B_4 of the end-effector in space is a cylindrical spiral, the equation of the trajectory of the

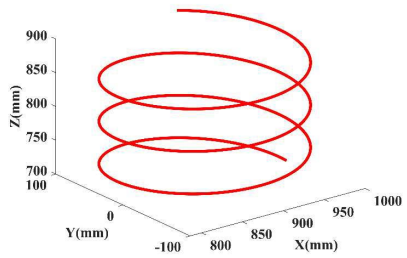

Fig. 8. Space spiral track.

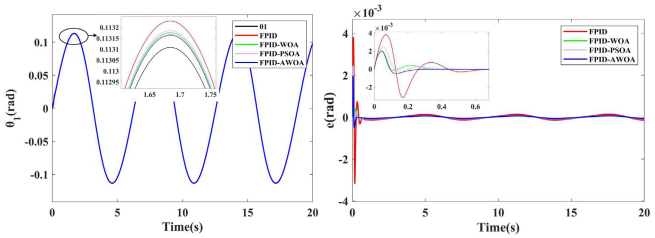

Fig. 9. Position tracking and the error of θ_1: (a) position tracking, and (b) the error.

end-effector is expressed as

$$\begin{cases} x = 100 \cdot cos(t) + 886 \\ y = 100 \cdot \sin(t) \\ z = 10t + 700 \end{cases} \tag{50}$$

where t is a certain point in a period.

The initial values of the fuzzy PID controller are set as K_{po}= 500, K_{io}= 10, and K_{do}= 10. The K_{e_j}, $K_{e_{cj}}$, $K_{u_{p_j}}$, $K_{u_{i_j}}$, and $K_{u_{d_j}}$ are optimized through WOA, PSOA, and AWOA. $\int_0^\infty e(t)^2 dt$ is selected as the fitness function. The population size is 10, the number of iterations is 100, the value range of ω is [0.6, 0.9], and the simulation time is 20s. The optimized values of K_{e_j}, $K_{e_{cj}}$, $K_{u_{p_j}}$, $K_{u_{i_j}}$, and $K_{u_{d_j}}$ based on WOA, PSOA, and AWOA are listed in TABLE I.

Position tracking and errors of θ_1, θ_2, and θ_3 in the joint space are shown in Figs. 9-11, and the trajectory tracking errors in the Cartesian space are shown in Fig. 12. According to Figs. 9-12, it can be seen that the four different control algorithms can achieve the smooth trajectory tracking. However, it is obvious that FPID-AWOA performs the best in terms of the stability and tracking accuracy. On one hand, according to Figs. 9-11 (b), the overshoot of FPID-AWOA is the smallest and only fluctuates once before reaching a stable state. The overshoot of FPID, FPID-WOA, and FPID-PSOA is higher than that of FPID-AWOA, and their fluctuation times are more than twice that of FPID-AWOA.

On the other hand, among the four control algorithms, FPID-AWOA takes the fastest time to reach stability. Moreover, in Cartesian space, FPID-AWOA ensures that the trajectory tracking errors and the times to reach stability of the X-axis, Y-axis, and Z-axis are less than that of FPID, FPID-WOA, and FPID-PSOA.

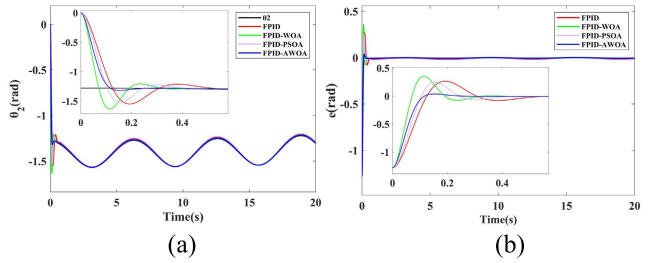

Fig. 10. Position tracking and the error of θ_2: (a) position tracking, and (b) the error.

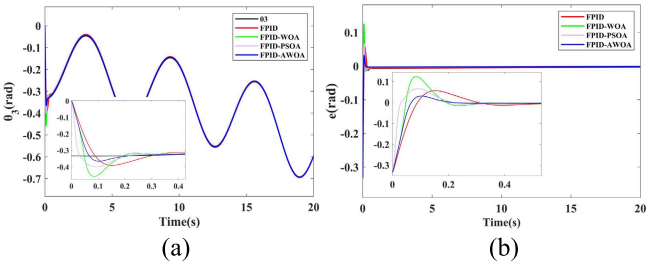

Fig. 11. Position tracking and the error of θ_3: (a) position tracking, and (b) the error.

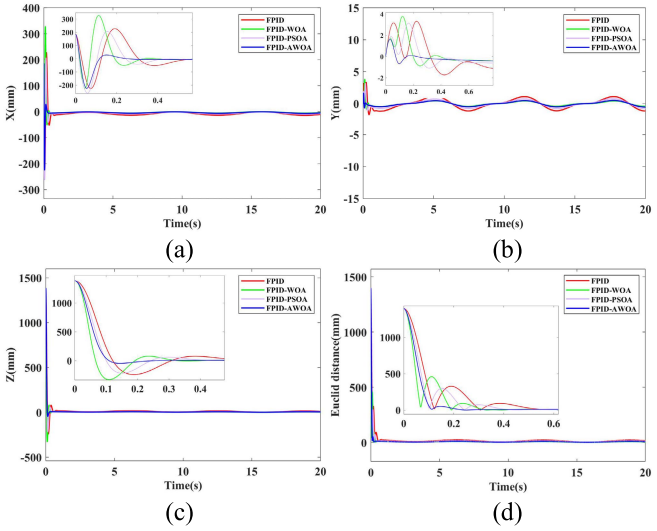

Fig. 12. The trajectory tracking errors in Cartesian space: (a) X-axis direction, (b) Y-axis direction, (c) Z-axis direction, and (d) the Euclid distance.

In order to quantitatively analyze and compare the control accuracy of the FPID, FPID-WOA, FPID-PSOA, and FPID-AWOA, the comparison of trajectory tracking performance under the four control algorithms are listed in TABLE II, the fluctuation ranges of errors along the X-axis, Y-axis, and Z-axis are listed in TABLE III, and the root-mean-square errors (RMSEs) [30], [31] along the X-axis, Y-axis, and Z-axis are listed in TABLE III. Note that the RMSE can be expressed as

$$RMSE = \sqrt{\frac{\sum (x - x_i)^2}{n}} \tag{51}$$

where x is the real value, which in this paper represents the ideal coordinate values of the X-axis, Y-axis, and Z-axis of the

TABLE I

(a) THE OPTIMIZED VALUES OF K_{e_j}, K_{ec_j}, K_{up_j}, K_{ui_j}, AND K_{ud_j}, AFTER WOA

	K_{e_j}	K_{ec_j}	K_{up_j}	K_{ui_j}	K_{ud_j}
θ_1	0	50.8484	59.3909	3.6067	10
θ_2	0.7537	0.1	100	10	4.22
θ_3	30	0.4882	50.0820	10	2.2685

(b) THE OPTIMIZED VALUES OF K_{e_j}, K_{ec_j}, K_{up_j}, K_{ui_j}, AND K_{ud_j}, AFTER PSOA

	K_{e_j}	K_{ec_j}	K_{up_j}	K_{ui_j}	K_{ud_j}
θ_1	1600	100	50.3515	9.1267	9.7327
θ_2	2.9585	0.1000	46.4408	1.7829	3.2350
θ_3	6.6358	0.0630	69.3497	10	0

(c) THE OPTIMIZED VALUES OF K_{e_j}, K_{ec_j}, K_{up_j}, K_{ui_j}, AND K_{ud_j}, AFTER AWOA

	K_{e_j}	K_{ec_j}	K_{up_j}	K_{ui_j}	K_{ud_j}
θ_1	1600	100	100	4.6798	9.1059
θ_2	0.6653	0.01	84.5972	4.4509	8.3741
θ_3	20.7795	0.4489	71.7043	7.8565	6.9237

TABLE II

(a) THE COMPARISON OF TRAJECTORY TRACKING PERFORMANCE OF θ_1 UNDER THE FOUR CONTROL ALGORITHMS

θ_1	Maximum overshoot of trajectory error/rad	Time to reach stability/s	Average error value after stabilization/rad
FPID	0.0038	0.7	0.0001
FPID-WOA	0.0021	0.35	0.00007
FPID-PSOA	0.0024	0.45	0.00008
FPID-AWOA	0.0019	0.25	0.00006

(b) THE COMPARISON OF TRAJECTORY TRACKING PERFORMANCE OF θ_2 UNDER THE FOUR CONTROL ALGORITHMS

θ_2	Maximum overshoot of trajectory error/rad	Time to reach stability/s	Average error value after stabilization/rad
FPID	0.2673	0.55	0.0048
FPID-WOA	0.3541	0.3	0.0020
FPID-PSOA	0.2493	0.4	0.0033
FPID-AWOA	0.0380	0.2	0.0013

(c) THE COMPARISON OF TRAJECTORY TRACKING PERFORMANCE OF θ_3 UNDER THE FOUR CONTROL ALGORITHMS

θ_3	Maximum overshoot of trajectory error/rad	Time to reach stability/s	Average error value after stabilization/rad
FPID	0.0571	0.55	0.0069
FPID-WOA	0.1245	0.45	0.0041
FPID-PSOA	0.0663	0.45	0.0036
FPID-AWOA	0.0314	0.3	0.0029

ideal trajectory; x_i is the measured value, which in this paper represents the coordinate values of the X-axis, Y-axis, and Z-axis measured during the simulation; and n is the number of measurements, which in this paper represents the number of times sampled during the simulation. In joint space, according to TABLE III, the performances of rotational angles tracking control are judged from three aspects: maximum overshoot of trajectory error, time to reach stability, and average error value after stabilization. For θ_1, in comparison with the FPID, FPID-WOA, and FPID-PSOA, the maximum overshoot of trajectory error is reduced by 50%, 9.5%, and 20.83%, the time to reach stability is accelerated by 64.29%, 28.57%, and 44.44%, the average error value after stabilization is reduced by 40%, 14.29%, and 25% by using the proposed FPID-AWOA. For θ_2, in comparison with the FPID, FPID-WOA, and FPID-PSOA, the maximum overshoot of trajectory error is reduced by 85.78%, 89.27% and 84.76%, the time to reach stability is accelerated by 63.64%, 33.33%, and 50%, the average error value after stabilization is reduced by 72.92%, 35% and 60.61% by using the proposed FPID-AWOA. For θ_3, in comparison with the FPID, FPID-WOA and FPID-PSOA, the maximum overshoot of trajectory error is reduced by 45.01%, 74.78%, and 52.64%, the time to reach stability is accelerated by 45.45%, 33.33%, and 33.33%, the average error value after stabilization is reduced by 57.97%, 29.27%, and 19.44% by using the proposed FPID-AWOA. The performance of trajectory tracking in the Cartesian space is reflected by the error fluctuation range and RMSE. According to the data in Tables III and IV, in comparison with the FPID, FPID-WOA, and FPID-PSOA in Cartesian space, the trajectory tracking error in the X-axis direction is reduced by 45%, 40.13%, and 37.22%, the trajectory tracking error in the Y-axis direction is reduced by 58.97%, 8.57%, and 39.62%, the trajectory tracking error in the Z-axis direction is reduced by 21.67%, 4.27%, and 11.41% by using the proposed FPID-AWOA, and the better stability is demonstrated by FPID-AWOA through the minimum fluctuation range. To sum up, it is precisely because of the weight function ω and differential mutation interference factor γ introduced by Eqs. (43) and (46) that AWOA improves the optimization accuracy and optimization speed, so that FPID-AWOA ensures the best stability and the highest accuracy among all control algorithms.

TABLE III

THE FLUCTUATION RANGES OF ERRORS ALONG THE X-AXIS, Y-AXIS, AND Z-AXIS AFTER STABILIZATION

	X-axis/mm	Y-axis/mm	Z-axis/mm
FPID	-14.2~-0.14	-1.13~1.14	2.12~19.38
FPID-WOA	-6.56~-0.22	-0.54~0.47	1.18~8.27
FPID-PSOA	-9.68~-1.19	-0.81~0.72	1.74~11.76
FPID-AWOA	-5.19~0.41	-0.41~0.44	0.43~7.67

TABLE IV

THE RMSES ALONG THE X-AXIS, Y-AXIS, AND Z-AXIS

	X-axis/mm	Y-axis/mm	Z-axis/mm
FPID	21.13	0.78	74.28
FPID-WOA	19.41	0.35	60.78
FPID-PSOA	18.51	0.53	65.67
FPID-AWOA	11.62	0.32	58.18

V. EXPERIMENT VALIDATION

In order to verify the effectiveness of the control algorithm proposed in this paper, a control experiment platform of the CDPR is built. The control experiment platform is shown in Fig. 13. The CDPR is controlled by Delta PLC. The control program is written by Delta software. The trajectory

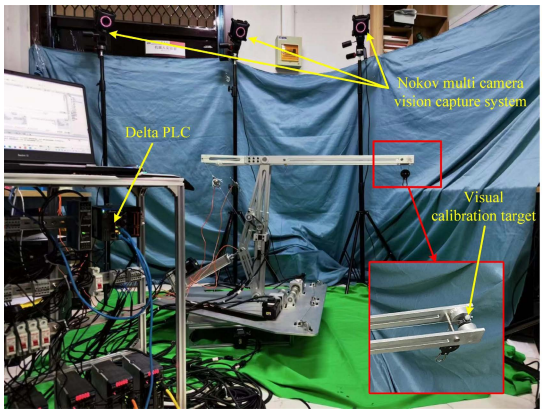

Fig. 13. The control experiment platform.

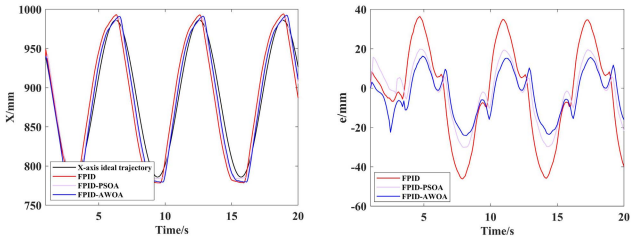

Fig. 14. Position tracking and the error in the X-axis direction in the spiral trajectory in the experiment: (a) position tracking, and (b) the error.

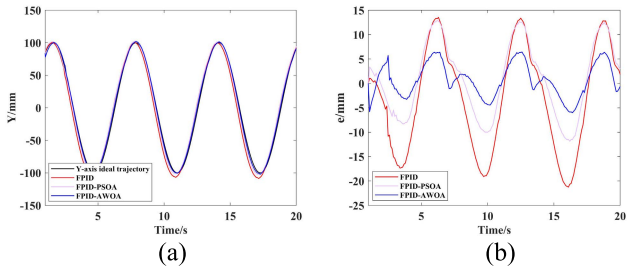

Fig. 15. Position tracking and the error in the Y-axis direction in the spiral trajectory in the experiment: (a) position tracking, and (b) the error.

of the CDPR is captured by the Nokov multi-camera visual capture system. The trajectory of the visual calibration target acquired by the camera is the end motion track of the CDPR.

Similar to the simulations, the spiral trajectory shown in Fig. 7 is used as the verification trajectory. Note that based on Eqs. (43) and (46) and the above simulation results, it is verified that FPID-AWOA performs better than FPID-WOA in terms of the stability, response speed, and tracking accuracy. In order to simplify the experiment, only the trajectory tracking experiments of FPID, FPID-PSOA, and FPID-WOA are selected for comparison. When the spiral trajectory is followed, position tracking and errors in the spiral trajectory in the experiment are shown in Figs. 14-16. According to Figs. 14-16, one can find that FPID-AWOA is closest to the ideal trajectory in the whole tracking process, and the fluctuation of the error is minimal. The approach of trajectory indicates high tracking accuracy and small error fluctuation

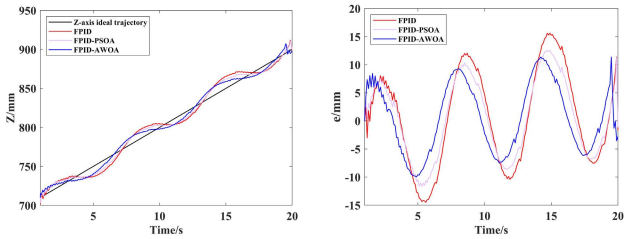

Fig. 16. Position tracking and the error in the Z-axis direction in the spiral trajectory in the experiment: (a) position tracking, and (b) the error.

TABLE V

THE FLUCTUATION RANGES OF THE ERRORS ALONG THE X-AXIS, Y-AXIS, AND Z-AXIS

	X-axis/mm	Y-axis/mm	Z-axis/mm
FPID	-46.2~36.41	-21.24~13.52	-14.5~15.61
FPID-PSOA	-30.2~19.86	-11.86~12.91	-11.7~12.61
FPID-AWOA	-24.1~16.23	-6.017~6.442	-9.97~11.38

TABLE VI

THE RMSES ALONG THE X-AXIS, Y-AXIS, AND Z-AXIS

	X-axis/mm	Y-axis/mm	Z-axis/mm
FPID	24.34	11.02	8.51
FPID-PSOA	14.41	7.56	6.93
FPID-AWOA	12.14	3.47	6.19

indicates strong stability. Hence, FPID-AWOA has the best control performance. The main reasons are the following two aspects. On one hand, K_{po}, K_{io}, and K_{do} in Eq. (31), the quantization factors K_{e_j} and $K_{e_{cj}}$, and the scale factors $K_{u_{pj}}$, $K_{u_{ij}}$, and $K_{u_{dj}}$ in the fuzzy controller are generally selected according to experience, which leads to the control effect of FPID being far worse than that of FPID-AWOA. On the other hand, the control performance of FPID-PSOA is similar to that of FPID-WOA based on simulations. According to Eqs. (43) and (46), ω and γ are introduced into AWOA, which makes the optimization performance of AWOA better than WOA; so FPID-AWOA is better than FPID-PSOA in the stability and tracking accuracy. Hence, FPID-AWOA effectively reduces all the errors in comparison with FPID and FPID-PSOA, and achieves the best control accuracy. Of course, the conclusions obtained in the experiment are also consistent with those in the numerical simulations.

Moreover, to quantitatively analyze and compare the control accuracy of the FPID, FPID-PSOA, and FPID-AWOA, the fluctuation ranges of the errors along the X-axis, Y-axis, and Z-axis are listed in Table III, and the RMSEs along the X-axis, Y-axis, and Z-axis are listed in Table III. In comparison with the FPID and FPID-PSOA, the trajectory tracking errors are reduced 51.2% and 19.5% on the X-axis, 64.2% and 49.7% on the Y-axis, and 29.1% and 12.2% on the Z-axis, respectively, by using the proposed FPID-AWOA, and the error fluctuation ranges of FPID-AWOA is the smallest, which reflects its better stability. These data more intuitively show the superiority of FPID-AWOA in the stability and accuracy of control. Of course, it is obvious that the

experimental results are not exactly the same as the simulation. Note that the difference between experiment and simulation is less than 15%. The reason is given as follows. Since the Matlab-based simulation is an ideal environment, the dynamic control in the simulation only depends on the given mathematical model and the Matlab solving accuracy of differential equations, and there is no external interference in Eq. (24) in the simulation. Therefore, in general, the dynamic control simulation can achieve very high accuracy. However, in actual experiments, the uncertainty of the robot dynamic model is inevitable, and an accurate dynamic model is almost impossible to obtain (for example, friction cannot be accurately modeled). In addition, there are also unavoidable disturbances in the dynamic control of actual robots, such as signal fluctuations, environmental disturbances, and so on. Therefore, the dynamic control in actual experiments cannot yield the same accuracy as the simulations, which is obvious and reasonable.

VI. Conclusion

In this paper, a fuzzy PID control strategy based on an adaptive whale optimization algorithm (FPID-AWOA) is presented for trajectory tracking of CDPR. On the basis of establishing the kinematics and dynamics model of CDPR, the problem that the dynamic equation is too complicated to express is solved by numerical method. Then, combined with the mechanical model and considering the experience of experts, a new fuzzy rule is proposed and a new fuzzy PID controller is designed. Subsequently, AWOA is used to optimize the quantization factors K_{e_j} and $K_{e_{cj}}$ and scale factors $K_{u_{pj}}$, $K_{u_{ij}}$, and $K_{u_{dj}}$ in the fuzzy PID controller. Note that, this paper improves AWOA by introducing weight and differential mutation interference factor on the basis of traditional WOA to improve the optimization performance of WOA. Numerical simulations demonstrate that compared with other control algorithms, FPID-AWOA can reduce all errors and significantly improve the control accuracy of CDPR in the joint space or the Cartesian space. Meanwhile, the trajectory tracking experiments were conducted on the constructed CDPR, which shows that compared with FPID and FPID-PSOA, the trajectory tracking errors are reduced 51.2% and 19.5% on the X-axis, 64.2% and 49.7% on the Y-axis, and 29.1% and 12.2% on the Z-axis, respectively, by using the proposed FPID-AWOA. Future research work will aim to extend the proposed approach to multiple CDPRs performing cooperative lifting tasks, which include not only static but also cooperative work while moving as well as obstacle avoidance.

References

[1] Z. Zhang et al., "State-of-the-art on theories and applications of cable-driven parallel robots," *Frontiers Mech. Eng.*, vol. 17, no. 3, p. 37, Sep. 2022.

[2] M. Wang, Y. Song, B. Lian, P. Wang, K. Chen, and T. Sun, "Dimensional parameters and structural topology integrated design method of a planar 5R parallel machining robot," *Mechanism Mach. Theory*, vol. 175, Sep. 2022, Art. no. 104964.

[3] L. Cuvillon, X. Weber, and J. Gangloff, "Modal control for active vibration damping of cable-driven parallel robots," *J. Mech. Robot.*, vol. 12, no. 5, Oct. 2020, Art. no. 051004.

[4] J. Gao, B. Zhou, B. Zi, S. Qian, and P. Zhao, "Kinematic uncertainty analysis of a cable-driven parallel robot based on an error transfer model," *J. Mech. Robot.*, vol. 14, no. 5, Feb. 2022, Art. no. 051008.

[5] D. Yun and R. S. Fearing, "Cockroach milli-robot with improved load capacity," *J. Mech. Robot.*, vol. 11, no. 3, Jun. 2019, Art. no. 035001.

[6] Y. Wang and Q. Xu, "Design and testing of a soft parallel robot based on pneumatic artificial muscles for wrist rehabilitation," *Sci. Rep.*, vol. 11, no. 1, pp. 1–11, Jan. 2021.

[7] Z. Lou, J. Zhang, R. Gao, L. Xu, K.-C. Fan, and X. Wang, "A 3D passive laser tracker for accuracy calibration of robots," *IEEE/ASME Trans. Mechatronics*, vol. 27, no. 6, pp. 5803–5811, Dec. 2022.

[8] V. Záda and K. Belda, "Structure design and solution of kinematics of robot manipulator for 3D concrete printing," *IEEE Trans. Autom. Sci. Eng.*, vol. 19, no. 4, pp. 3723–3734, Oct. 2022.

[9] M. Xiao, Y. Ding, and G. Yang, "A model-based trajectory planning method for robotic polishing of complex surfaces," *IEEE Trans. Autom. Sci. Eng.*, vol. 19, no. 4, pp. 2890–2903, Oct. 2022.

[10] R. Chai, D. Liu, T. Liu, A. Tsourdos, Y. Xia, and S. Chai, "Deep learning-based trajectory planning and control for autonomous ground vehicle parking maneuver," *IEEE Trans. Autom. Sci. Eng.*, vol. 20, no. 3, pp. 1633–1647, Jul. 2022.

[11] H. Wang, J. Kinugawa, and K. Kosuge, "Exact kinematic modeling and identification of reconfigurable cable-driven robots with dual-pulley cable guiding mechanisms," *IEEE/ASME Trans. Mechatronics*, vol. 24, no. 2, pp. 774–784, Apr. 2019.

[12] H. Jia, W. Shang, F. Xie, B. Zhang, and S. Cong, "Second-order sliding-mode-based synchronization control of cable-driven parallel robots," *IEEE/ASME Trans. Mechatronics*, vol. 25, no. 1, pp. 383–394, Feb. 2020.

[13] Y. Wang, F. Yan, J. Chen, F. Ju, and B. Chen, "A new adaptive time-delay control scheme for cable-driven manipulators," *IEEE Trans. Ind. Informat.*, vol. 15, no. 6, pp. 3469–3481, Jun. 2019.

[14] G. Hao et al., "A deep deterministic policy gradient approach for vehicle speed tracking control with a robotic driver," *IEEE Trans. Autom. Sci. Eng.*, vol. 19, no. 3, pp. 2514–2525, Jun. 2021.

[15] V. K. Nguyen, H. T. Pham, H. H. Pham, and Q. K. Dang, "Optimization design of a compliant linear guide for high-precision feed drive mechanisms," *Mechanism Mach. Theory*, vol. 165, Nov. 2021, Art. no. 104442.

[16] W. Wang, J. Ma, X. Li, H. Zhu, C. W. da Silva, and T. H. Lee, "Hybrid active–passive robust control framework of a flexure-joint dual-drive gantry robot for high-precision contouring tasks," *IEEE Trans. Ind. Electron.*, vol. 70, no. 2, pp. 1676–1686, Feb. 2023.

[17] R. Prakash, L. Behera, S. Mohan, and S. Jagannathan, "Dual-loop optimal control of a robot manipulator and its application in warehouse automation," *IEEE Trans. Autom. Sci. Eng.*, vol. 19, no. 1, pp. 262–279, Jan. 2022.

[18] S. Purwar, I. N. Kar, and A. N. Jha, "Adaptive control of robot manipulators using fuzzy logic systems under actuator constraints," *Fuzzy Sets Syst.*, vol. 152, no. 3, pp. 651–664, Jun. 2005.

[19] M. J. Mahmoodabadi, M. B. S. Mottaghi, and A. Mahmodinejad, "Optimum design of fuzzy controllers for nonlinear systems using multi-objective particle swarm optimization," *J. Vib. Control*, vol. 22, no. 3, pp. 769–783, Feb. 2016.

[20] R. Sharma, K. P. S. Rana, and V. Kumar, "Performance analysis of fractional order fuzzy PID controllers applied to a robotic manipulator," *Expert Syst. Appl.*, vol. 41, no. 9, pp. 4274–4289, Jul. 2014.

[21] X. Liang, H. Wang, Y.-H. Liu, B. You, Z. Liu, and W. Chen, "Calibration-free image-based trajectory tracking control of mobile robots with an overhead camera," *IEEE Trans. Autom. Sci. Eng.*, vol. 17, no. 2, pp. 933–946, Apr. 2020.

[22] R. Sharma, K. P. S. Rana, and V. Kumar, "Statistical analysis of GA based PID controller optimization for robotic manipulator," in *Proc. Int. Conf. Issues Challenges Intell. Comput. Techn. (ICICT)*, Ghaziabad, India, Feb. 2014, pp. 713–718.

[23] A. O. Pizarro-Lerma, R. García-Hernández, and V. A. Santibáñez, "Fine-tuning of a fuzzy computed-torque control for a 2-DOF robot via genetic algorithms," *IFAC-PapersOnLine*, vol. 51, no. 13, pp. 326–331, 2018.

[24] Y. Hu, Y. Yang, S. Li, and Y. Zhou, "Fuzzy controller design of micro-unmanned helicopter relying on improved genetic optimization algorithm," *Aerosp. Sci. Technol.*, vol. 98, Mar. 2020, Art. no. 105685.

[25] X. Shao, G. Sun, W. Yao, J. Liu, and L. Wu, "Adaptive sliding mode control for quadrotor UAVs with input saturation," *IEEE/ASME Trans. Mechatronics*, vol. 27, no. 3, pp. 1498–1509, Jun. 2022.

[26] G. Sun, L. Wu, Z. Kuang, Z. Ma, and J. Liu, "Practical tracking control of linear motor via fractional-order sliding mode," *Automatica*, vol. 94, pp. 221–235, Aug. 2018.

[27] C. Yang, Y. Jiang, J. Na, Z. Li, L. Cheng, and C.-Y. Su, "Finite-time convergence adaptive fuzzy control for dual-arm robot with unknown kinematics and dynamics," *IEEE Trans. Fuzzy Syst.*, vol. 27, no. 3, pp. 574–588, Mar. 2019.

[28] S. Zhang, Y. Wu, X. He, and Z. Liu, "Cooperative fault-tolerant control for a mobile dual flexible manipulator with output constraints," *IEEE Trans. Autom. Sci. Eng.*, vol. 19, no. 4, pp. 2689–2698, Oct. 2022.

[29] N. Sun, Y. Fu, T. Yang, J. Zhang, Y. Fang, and X. Xin, "Nonlinear motion control of complicated dual rotary crane systems without velocity feedback: Design, analysis, and hardware experiments," *IEEE Trans. Autom. Sci. Eng.*, vol. 17, no. 2, pp. 1017–1029, Apr. 2020.

[30] H. Ji, W. Shang, and S. Cong, "Adaptive synchronization control of cable-driven parallel robots with uncertain kinematics and dynamics," *IEEE Trans. Ind. Electron.*, vol. 68, no. 9, pp. 8444–8454, Sep. 2021.

[31] O. Özgüner et al., "Camera-robot calibration for the da Vinci robotic surgery system," *IEEE Trans. Autom. Sci. Eng.*, vol. 17, no. 4, pp. 2154–2161, May 2020.

Bin Zhou received the bachelor's, master's, and Ph.D. degrees from the Hefei University of Technology, Hefei, China, in 2012, 2015, and 2019, respectively.

From 2017 to 2019, he was a Visiting Scholar with the Department of Mechanical Engineering, University of Maryland Baltimore County, Baltimore, MD, USA. He is currently a Lecturer with the School of Mechanical Engineering, Hefei University of Technology. His research interests include uncertainty analysis and reliability-based optimization design, and intelligent control of cable-driven parallel robots.

Yuhang Wang received the bachelor's degree from Shanghai Second Polytechnic University in 2020. He is currently pursuing the M.E. degree in mechanical engineering with the Hefei University of Technology, Hefei, China.

His research interests include adaptive dynamic control and visual servoing control of cable-driven parallel robots.

Bin Zi received the Ph.D. degree in mechatronic engineering from Xidian University, China, in 2007. He was a Visiting Scholar with the Chair of Mechanics and Robotics, University of Duisburg-Essen, Germany, from 2011 to 2012, and a Visiting Professor with the Robotics and Automation Laboratory, Institute of Technology, University of Ontario, Canada, in 2015. He is currently the Dean and a Full Professor with the School of Mechanical Engineering, and the Director of the Robotics Institute, Hefei University of Technology, China. His research interests include the theory, technology and equipment of rigid-flexible coupling intelligent robots, control and automation of intelligent manufacturing systems, and multi-robot systems. He received the National Science Fund for Distinguished Young Scholars of China. He is an Associate Editor of *ASME Journal of Mechanical Design* and an Editorial Board Member of the *Chinese Journal of Mechanical Engineering*, *International Journal of Mechanical Sciences*, *Robotics*, and *Journal of Control and Decision*.

Weidong Zhu received the dual B.S. degrees in mechanical engineering and computational science from Shanghai Jiao Tong University, Shanghai, China, in 1986, the M.S. degree in mechanical engineering from Arizona State University, Tempe, AZ, USA, in 1988, and the Ph.D. degree in mechanical engineering from the University of California at Berkeley, Berkeley, CA, USA, in 1994.

He is a fellow of the American Society of Mechanical Engineers. He has served as an Associate Editor for the *Journal of Vibration and Acoustics* (ASME) and the *Journal of Dynamic Systems, Measurement and Control* (ASME), and a Subject Editor for the *Journal of Sound and Vibration* and *Nonlinear Dynamics*.